The Space Filling Mode of Holey Fibers: An Analytical Vectorial Solution

Michele Midrio, Mukesh P. Singh, and Carlo G. Someda

***Abstract*—We tackle holey fibers in full vectorial terms. From Maxwell's equations, we derive the dispersion relations of the modes guided by an infinitely self-similar air hole lattice. We focus in particular on the fundamental mode (the so-called space filling mode), and show that previous numerical results based on vector methods are accurate, but scalar ones are not. We also find the field flow lines, intensity distribution in the cross section, and linear polarization ratio vs. wavelegth.**

***Index Terms*—Electromagnetic propagation in nonhomogeneous media, optical fibers, optical fiber cladding, optical fiber theory.**

I. Introduction

HOLEY fibers are fibers in which the field confinement is obtained by means of a suitable pattern of circular air holes, around a central zone of pure silica glass. As well known, light guidance in such fibers may stem from two different physical processes. The first one is the so-called *photonic bandgap* effect: the air hole pattern is designed to form a honeycomb lattice, which stops propagation in any transverse direction. Light can travel just along the longitudinal direction, close to a defect introduced on purpose in the lattice [1]–[3]. The second mechanism guides light without resorting to band-gap effects. It is usually referred to as *total internal reflection* (TIR). Basically, the air hole pattern simply yields a lower *effective* refractive index, compared to the physical index of the central pure silica zone. The guidance mechanism is then essentially the same as in conventional fibers, the lattice acting as the cladding [4], [6]. TIR fibers are usually designed and fabricated with a hexagonal air hole lattice, but this geometry is not strictly necessary: any arrangement of air holes in a silica matrix would yield a reduced effective index.

The value of the cladding effective index is a very important design parameter. It sets the width of the spectral range over which a holey fiber is single-mode [4]. So far, computation of the cladding effective index has been performed by using either full-vectorial numerical techniques [3], [7], [8], or approximate scalar analytical approaches [4]. Numerical techniques require large CPU times and memory allocations. As for scalar approaches, we will show in this paper that at least some of them yield effective index values that differ significantly from those computed using more precise vector methods. Altogether, there is plenty of space for trying new approaches.

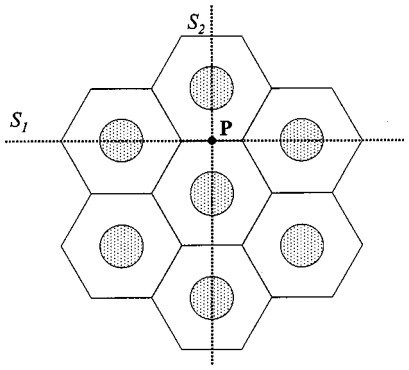

Fig. 1. Schematic diagram of the infinitely self similar hexagonal lattice. The dashed lines labeled as S_1 and S_2 represent planes of symmetry of the structure.

In this paper, we show that the cladding effective index can be evaluated using a fully analytical vector approach. While our target is the so-called *space filling mode* (i.e., the fundamental cladding mode) of a holey fiber, the tool that we use to this purpose is an infinetely self-similar hexagonal lattice. We will show how to find closed-form dispersion relations for the modes of this structure. We will also present information on the modal field: flow lines, amplitude contour plots and polarization ratio of the transverse electric field. As far as we know, these results are new. Indeed, so far very few analytical results have been published in the whole theory of photonic crystals and holey fibers. Our results appear to yield an improved physical insight on items that affect in depth the design of single-mode holey fibers.

II. Symmetry Properties of the Hexagonal Lattice

The exact solutions of Maxwell's equations in a hexagonal lattice can be chased on the grounds of simple symmetry properties. Let us focus on the point P in Fig. 1. There are two planes of symmetry, marked S_1 and S_2, through P. Fields which exhibit either an odd or an even parity with respect to either S_1 or S_2 are unaffected if their symmetry plane is replaced either by a perfect electric or by a perfect magnetic conductor. For the longitudinal components of the electric and magnetic field this translates as follows ($\hat{z}$ is the unit vector orthogonal to the lattice plane):

Manuscript received November 30, 1999; revised March 2, 2000. The work of M. P. Singh was supported by the "ASICTP Programme for Training and Research in Italian Laboratories, Trieste, Italy."

M. Midrio is with the Dipartimento di Ingegneria Elettrica Gestionale e Meccanica, Istituto Nazionale per la Fisica della Materia, Università degli Studi di Udine, Udine 33100, Italy.

M. P. Singh is with the Dipartimento di Elettronica e Informatica, Università degli Studi di Padova, 35131 Padova, Italy, on leave from Department of Applied Sciences and Humanities, Faculty of Engineering and Technology, Jamia Millia Islamia, Jamia Nagar, New Delhi 110025, India.

C. G. Someda is with the Dipartimento di Elettronica e Informatica, Università degli Studi di Padova, Padova 35131, Italy.

Publisher Item Identifier S 0733-8724(00)05768-6.

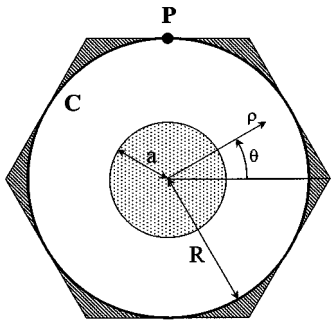

Fig. 2. Schematic diagram of the sinlge cell in the hexagonal lattice. The circle C is the circle where boundary conditions due to symmetry properties have to be applied. ρ and θ are transverse coordinates of a cylindrical reference frame centered on the cell axis.

1) $E_z(P) = 0$, if S_1 and/or S_2 are perfect electric conductors;
2) $H_z(P) = 0$, if S_1 and/or S_2 are perfect magnetic conductors;
3) $E_z(P) = 0$ *and* $H_z(P) = 0$, if S_1 is a perfect magnetic conductor and S_2 a perfect electric conductor, or vice-versa.

Cases 1 and 2 entail a field with a quadrant-like symmetry (not necessarily a *perfect* quadrant symmetry, but still a pronounced resemblance of the field in the four quadrants). This is not compatible with the fundamental mode, which, as frequency $\omega \to 0$, must tend to a uniform plane wave. In fact, note that the lattice is not invariant under a 90° rotation: the planes S_1 and S_2 are not equivalent to each other. These remarks imply that the lattice fundamental mode must be a field for which S_1 is an electric conductor and S_2 a magnetic conductor, or vice-versa, in any case, a field having

$$E_z(P) = H_z(P) = 0. \tag{1}$$

We will add further remarks on this point at the end of the next section, after deriving the dispersion relations for the three sets of modes which correspond to the three types of boundary conditions that we listed above.

We focus now on the unit cell of the infinitely self-similar lattice, and use the cylindrical frame $\{\hat{\rho}, \hat{\theta}, \hat{z}\}$ shown in Fig. 2. Let us resort to separation of variables. This step is not rigorous: in general, the field in the unit cell can be expressed as a series of cylindrical harmonics, each of which has its own ρ and θ dependencies. However, let us stress that we are looking for the fundamental space-filling mode. As we said shortly, it must tend to a plane wave when the wavelength becomes large compared to the lattice pitch, so, its content of higher order cylindrical harmonics must be small. Bearing this in mind, we write the E_z and H_z field components as

$$\begin{aligned} H_z(\rho, \theta, z) &= Q_\ell(\rho) e^{i\ell\theta} e^{-\gamma z} \\ E_z(\rho, \theta, z) &= R_\ell(\rho) e^{i\ell\theta} e^{-\gamma z}. \end{aligned} \tag{2}$$

Although we do not know yet which value of ℓ will correspond to the fundamental mode, we note that, as $\exp\{i\ell\theta\} \neq 0$, for any ℓ, (1) entails $E_z(\rho = R) = H_z(\rho = R) \equiv 0$ over the whole circle C, once we accept that they hold in P for a field of the form of (2).

As correctly pointed out by two referees, this procedure—i.e., to derive (1) from symmetry considerations and then assume that the field is like (2)—does justify the adoption of those boundary conditions ($E_z(\rho = R) = H_z(\rho = R) \equiv 0$) over a *circle*, but leaves some doubts about the choice of $R = \Lambda/2$ as the *radius* of this circle, Λ being the pitch of the hexagonal lattice. In particular, at first sight this choice seems to underestimate the "filling factor" (defined as the fraction of glass area to the total area of the honeycomb cell), as it neglects the corners of the hexagon (shaded regions in Fig. 2. When we get to numerical examples (Fig. 4) in Section IV), we will see that, in fact, the choice $R = \Lambda/2$ yields results in surprisingly good agreement with very precise numerical methods, while if we choose another value for R, aiming at preserving the filling factor of the original hexagon, the agreement gets worse.

From now on, all our steps will be rigorous, without any further approximation or assumption. To make our approach as general as possible, we will derive dispersion relations not only for the fundamental mode, but also for the other modes. Still, for higher order modes we do not have any criterion, for the time being, to establish what level of inaccuracy has been introduced by the separation of variables. At the end, we will know the field only inside the circle C. To pass from it to the field in the infinitely self-similar lattice will be a simple matter of common sense.

III. Dispersion Relations

In the cylindrical frame of Fig. 2, the e.m. field within the unit cell can be written as

$$\begin{cases} \mathbf{E}_j(\rho, \theta, z) = \vec{\mathcal{E}}_j(\rho, \theta) e^{-\gamma z} \\ \mathbf{H}_j(\rho, \theta, z) = \vec{\mathcal{H}}_j(\rho, \theta) e^{-\gamma z} \end{cases}, \quad j = 1, 2$$

where $j = 1$ for quantities defined in the $0 \leq \rho \leq a$ region, $j = 2$ in $a \leq \rho \leq R$. We use a similar notation for refractive indices n_1, n_2, with $n_1 < n_2$. The transverse fields $\{\vec{\mathcal{E}}_t, \vec{\mathcal{H}}_t\}$ may be written as [9]

$$\vec{\mathcal{E}}_{tj} = -\frac{1}{\gamma^2 - \sigma_j^2} \{\gamma \nabla_t \mathcal{E}_{zj} + i\omega\mu \nabla_t \mathcal{H}_{zj} \times \hat{z}\}, \quad j = 1, 2 \tag{3}$$

$$\vec{\mathcal{H}}_{tj} = -\frac{1}{\gamma^2 - \sigma_j^2} \{\gamma \nabla_t \mathcal{H}_{zj} - i\omega\epsilon_j \nabla_t \mathcal{E}_{zj} \times \hat{z}\}, \quad j = 1, 2 \tag{4}$$

where $\sigma_j^2 = -\omega^2 \mu \epsilon_j$, $\nabla_t = \hat{\rho}\partial/(\partial\rho) + \hat{\theta}/(1/\rho)\partial/\partial\theta$, and $\mathcal{E}_{zi}$, $\mathcal{H}_{zi}$ are two independent solutions of a 2-D Helmholtz equation [9]. At $\rho = a$, continuity of tangential components reads

$$\begin{aligned} \mathcal{E}_{z1}(\rho = a, \theta) &= \mathcal{E}_{z2}(\rho = a, \theta) \\ \mathcal{H}_{z1}(\rho = a, \theta) &= \mathcal{H}_{z2}(\rho = a, \theta) \\ \mathcal{E}_{\theta 1}(\rho = a, \theta) &= \mathcal{E}_{\theta 2}(\rho = a, \theta) \\ \mathcal{H}_{\theta 1}(\rho = a, \theta) &= \mathcal{H}_{\theta 2}(\rho = a, \theta). \end{aligned}$$

Boundary conditions to be applied at $\rho = R$ in case 1 (electric conductor) read

$$\mathcal{E}_{z2}(\rho = R, \theta) \equiv 0, \quad \left.\frac{\partial \mathcal{H}_{z2}}{\partial \rho}\right|_{\rho = R, \theta} \equiv 0$$

and in case 2 (magnetic conductor)

$$\mathcal{H}_{z2}(\rho=R,\theta)\equiv 0,\quad \left.\frac{\partial\mathcal{E}_{z2}}{\partial\rho}\right|_{\rho=R,\theta}\equiv 0.$$

For case 3—the most interesting one, because we will see that it encompasses the fundamental mode—they read

$$\mathcal{E}_{z2}(\rho=R,\theta)\equiv 0,\quad \mathcal{H}_{z2}(\rho=R,\theta)\equiv 0.$$

We can now derive the dispersion relations. To gain space, we will show details only for the perfect magnetic wall. This is not the most practical case because, as we just said, it does not encompass the fundamental mode. Still, we prefer to show details on it, rather than on the case of (3), because it is much simpler in terms of mathematics. Dispersion relations for the other cases will just be quoted, leaving their derivation to the interested reader.

The solutions of the 2-D Helmholtz equation which satisfy the magnetic-conductor boundary conditions are

$$\begin{aligned}\mathcal{H}_{z1}(\rho,\theta)&=H_1 I_\ell\left(w\frac{\rho}{a}\right)e^{i\ell\theta}\\ \mathcal{E}_{z1}(\rho,\theta)&=E_1 I_\ell\left(w\frac{\rho}{a}\right)e^{i\ell\theta}\\ \mathcal{H}_{z2}(\rho,\theta)&=H_2 Q_\ell(\rho)e^{i\ell\theta}\\ \mathcal{E}_{z2}(\rho,\theta)&=E_2 P_\ell(\rho)e^{i\ell\theta}\end{aligned}$$

where E_1, E_2, H_1 and H_2 are complex amplitude coefficients, to be determined later, $\ell=0,\pm1,\ldots$

$$P_\ell(\rho)=J_\ell(u\rho/a)Y_\ell(uR/a)-Y_\ell(u\rho/a)J_\ell(uR/a)$$

and

$$Q_\ell(\rho)=J_\ell(u\rho/a)\,Y'_\ell(\xi)|_{\xi=uR/a}-Y_\ell(u\rho/a)\,J'_\ell(\xi)|_{\xi=uR/a}$$

with $J_\ell(\cdot)$ and $Y_\ell(\cdot)$ the ℓ-th order Bessel functions of first and second kind, respectively, and $I_\ell(\cdot)$ the ℓ-th order modified Bessel function of the first kind. Primes denote derivatives with respect to the argument, and $w^2=\omega^2(n_{\text{eff}}^2-n_1^2)a^2/c^2, u^2=\omega^2(n_2^2-n_{\text{eff}}^2)a^2/c^2$ with $\beta=(\omega/c)n_{\text{eff}}=-i\gamma$ the unknown phase constant to be determined.

Replacing these expressions into (3), (4), and applying the continuity conditions, we find a system of four linear homogenenous equations, in the four unknown amplitudes E_1, H_1, E_2, H_2. For a nontrivial solution, it is necessary that $\det\mathbf{M}=0$, where $\mathbf{M}$ is the matrix of the linear system coefficients. This yields the characteristic equation in the unknown β. For instance, let us take the case $\ell=0$, where the 4×4 system splits into two independent 2×2 systems, one in H_1 and H_2, one in E_1 and E_2 only.

These two independent sets of equations correspond to transverse electric (TE) and transverse magnetic (TM) modes, respectively, with characteristic equations

$$\begin{aligned}i'_0(w)&=-p'_0(u)\quad \text{TE}^{(M)}\text{ modes}\\ \epsilon_{r1}i'_0(w)&=-\epsilon_{r2}q'_0(u)\quad \text{TM}^{(M)}\text{ modes}\end{aligned}$$

where

$$i'_\ell(w)=\frac{I'_\ell(w)}{wI_\ell(w)},\quad p'_\ell(u)=\frac{P'_\ell(u)}{uP_\ell(\rho=a)},$$
$$q'_\ell(u)=\frac{Q'_\ell(u)}{uQ_\ell(\rho=a)}$$

with

$$P'_\ell(u)=\frac{a}{u}\left.\frac{\partial P_\ell(\rho)}{\partial\rho}\right|_{\rho=a},\quad Q'_\ell(u)=\frac{a}{u}\left.\frac{\partial Q_\ell(\rho)}{\partial\rho}\right|_{\rho=a}.$$

The superscript M reminds us that we are dealing with a structure bounded by a magnetic wall.

Not surprisingly, the equations we found are reminiscent of those which apply to step-index fibers [9]. This device and its well-known solution can be used as a checkpoint, to test the validity of the results that we derived here. To this purpouse, let $R\to\infty$, and interchange n_1 with n_2 (refractive index in the inner region higher than in the outer region). Let $U^2=-w^2$ and $W^2=-u^2$. We find then

$$\frac{I'_0(w)}{wI_0(w)}=-\frac{J'_0(U)}{UJ_0(U)}$$

and

$$\lim_{R\to\infty}\frac{J'_0(u)Y_0(uR/a)-Y'_0(u)J_0(uR/a)}{u(J_0(u)Y_0(uR/a)-Y_0(u)J_0(uR/a)}=-\frac{K'_0(W)}{WK_0(W)}$$

and the characteristic equation of TE modes becomes $J'_0(U)/(UJ_0(U))=-K'_0(W)/(WK_0(W))$, i.e. that of TE modes of a step-index dielectric waveguide.

For $\ell\neq0$, the 4×4 system does not split into two independent subsystems. The corresponding modes are *hybrid*, like in step-index fibers. Defining the quantity $v^2=u^2+w^2=\omega^2/c^2a^2(n_2^2-n_1^2)$ ($v=$ normalized frequency), and going then through some lengthy but trivial algebra, very similar to that of [9], the characteristic equation can be shown to read

$$[i'_\ell(w)+p'_\ell(u)]\,[\epsilon_{r1}i'_\ell(w)+\epsilon_{r2}q'_\ell(u)]=f^2(u,w,\ell)\qquad(5)$$

where

$$f^2(u,w,\ell)=\ell^2\left(\frac{1}{u^2}+\frac{1}{w^2}\right)\left(\frac{\epsilon_{r1}}{w^2}+\frac{\epsilon_{r2}}{u^2}\right).$$

Equation (5) can then be solved numerically, to find the effective index of the modes which are bounded by a perfect magnetic conductor.

The dispersion relations for the two remaining sets of modes can be derived in a very similar way. In fact, the perfect electric wall can be dealt with simply replacing Q_ℓ with P_ℓ, and viceversa, in the previous steps, so the dispersion relations is

$$\begin{aligned}i'_0(w)&=-q'_0(u)\quad \text{TE}^{(E)}\text{ modes}\\ \epsilon_{r1}i'_0(w)&=-\epsilon_{r2}p'_0(u)\quad \text{TM}^{(E)}\text{ modes}\end{aligned}$$

for $\ell=0$, and

$$[i'_\ell(w)+q'_\ell(u)]\,[\epsilon_{r1}i'_\ell(w)+\epsilon_{r2}p'_\ell(u)]=f^2(u,w,\ell)\qquad(6)$$

for $\ell\neq0$.

For the most interesting case, namely an electric and a magnetic symmetry plane, the dispersion relations can be found from the previous ones noticing that Q_ℓ has to be replaced by P_ℓ, *not vice-versa*. Hence, the characteristic equations read

$$i_0'(w) = -p_0'(u) \quad \mathrm{TE}^{(T)} \text{ modes}$$
$$\epsilon_{r1} i_0'(w) = -\epsilon_{r2} p_0'(u) \quad \mathrm{TM}^{(T)} \text{ modes}$$

for $\ell = 0$, and

$$[i_\ell'(w) + p_\ell'(u)]\,[\epsilon_{r1} i_\ell'(w) + \epsilon_{r2} p_\ell'(u)] = f^2(u, w, \ell) \qquad (7)$$

for $\ell \neq 0$. The superscript T reminds us that we are dealing with the case where the whole electromagnetic (EM)-field is, on the outer circle C, transverse with respect to the direction of propagation. Incidentally, the characteristic equation of $\mathrm{TE}^{(T)}$ modes coincides with that of $\mathrm{TE}^{(M)}$ modes. This is not an occasional coincidence: by definition, the longitudinal electric field of TE modes is zero everywhere, including the outer circle. Therefore, $\mathrm{TE}^{(M)}$ modes and $\mathrm{TE}^{(T)}$ modes satisfy *de facto* the same boundary conditions on the outer circle. Similarly, the characteristic equations of $\mathrm{TM}^{(T)}$ modes and $\mathrm{TM}^{(E)}$ modes are the same.

It is easy to check that (5)–(7) are invariant with respect to the change $\ell \to -\ell$. Hence, any of their solutions corresponds to a pair of degenerate modes. This allows us to assume $\ell > 0$ from now on.

IV. Hybrid Modes: The Fundamental Mode

Our purpose is now to identify the fundamental mode, among all the solutions of the characteristic equations found in the previous section. Let us first show that their solutions can be divided into two sets, analogous to the HE and EH modes of step-index fibers. To this end, we regard (5)–(7) as second-order algebraic equations in i_ℓ', solve them, and then use Bessel function recurrence relations, following a procedure whose rather lengthy details can be found in [9, pp. 381–385]. The final results are

$$\frac{I_{\ell+1}(w)}{I_\ell(w)} = -\frac{\ell}{w} - \frac{w}{2}\left(A_\ell' + \frac{\epsilon_{r2}}{\epsilon_{r1}} B_\ell'\right) - w\sqrt{\frac{1}{4}\left(A_\ell' - \frac{\epsilon_{r2}}{\epsilon_{r1}} B_\ell'\right)^2 + \frac{f^2(u,w,\ell)}{\epsilon_{r1}}} \qquad (8)$$

and

$$\frac{I_{\ell-1}(w)}{I_\ell(w)} = \frac{\ell}{w} - \frac{w}{2}\left(A_\ell' + \frac{\epsilon_{r2}}{\epsilon_{r1}} B_\ell'\right) + w\sqrt{\frac{1}{4}\left(A_\ell' - \frac{\epsilon_{r2}}{\epsilon_{r1}} B_\ell'\right)^2 + \frac{f^2(u,w,\ell)}{\epsilon_{r1}}} \qquad (9)$$

where the quantities called A_ℓ' and B_ℓ' are functions of u, and read

$$A_\ell'(u) = p_\ell'(u), \quad B_\ell'(u) = q_\ell'(u) \quad \text{for ``M'' modes}$$
$$A_\ell'(u) = q_\ell'(u), \quad B_\ell'(u) = p_\ell'(u) \quad \text{for ``E'' modes}$$
$$A_\ell'(u) = B_\ell'(u) = p_\ell'(u) \quad \text{for ``T'' modes.}$$

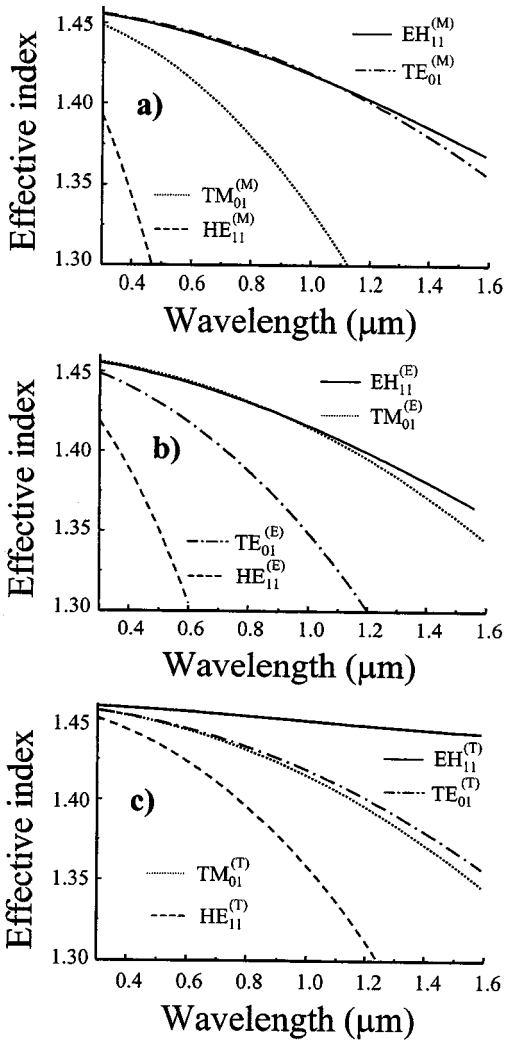

Fig. 3. Dispersion curves for some of the modes allowed to propagate in the lattice. Plate (a) refers to modes bounded by a perfect magnetic conductor. Whereas plates (b) and (c) refers to the case of modes bounded by a perfect electric conductor, and by a surface imposing null values to the longitudinal component of both the electric and the magnetic field. In all the plates, solid line is for the EH_{11} mode, dashed line for the HE_{11} mode, dotted line for the TM_{01} mode, and dashed-dotted line for the TE_{01} mode.

By analogy with step-index fibers, we will call "EH" those modes which correspond to solutions of (8), "HE" those which correspond to solutions of (9).

The space filling mode of the hexagonal lattice is, by definition, that solution, among all those we found so far, which exhibits the highest effective index. Analogy with step-index fibers might be misleading; to be on the safe side, we prefer to identify it by solving numerically (8), (9), with the three possible boundary conditions listed above. We choose the following parameters, that correspond to an example already available in the literature [8]: an air-silica hexagonal lattice where the radius of the air holes is $a = 0.3\ \mu$m; the distance between centers of neighboring holes (or lattice pitch) is $\Lambda = 2.3\ \mu$m, so $R = 1.15\ \mu$m. The refractive index of silica is taken to be $n_2 = 1.46$.

Dispersion curves for some low-order modes are shown in Fig. 3, where part a) refers to "M" modes, part b) to "E" modes,

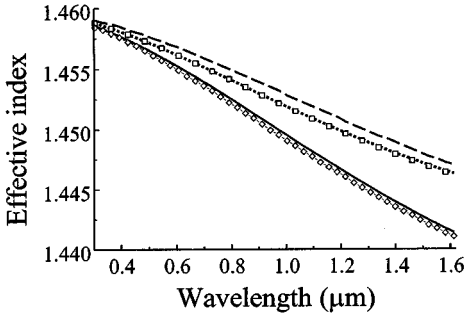

Fig. 4. Dispersion relation for the fundamental $EH_{11}(T)$ mode (solid), as compared to numerically computed SFM effective index (open diamonds, after Ref. [8]). The dashed line is the dispersion relation computed by imposing the boundary condition on the circle passing through the hexagon vertices). The two remaining curves give the SFM effective index, as computed on the basis of a scalar approach. The dotted line is the effective index following [4], the open squares give the index computed by means of a scalar finite-difference code.

and part c) to "T" modes. We see that, in agreement with the intuitive arguments developed in Section 2, the fundamental mode belongs to the "T" set. In particular, it is the $EH_{11}^{(T)}$ mode. The space filling mode of the lattice is then a two-fold degenerate mode. This point will be dealt with again in the next Section, where we show field flow lines and amplitude contour plots.

Fig.4 is an expanded view of the dispersion curve, where the $EH_{11}^{(T)}$-mode effective index found in this way (for two choices of the radius R of the circle where we impose the boundary conditions) is compared with results calculated using two previously published methods. We see that there is very good agreement between our results corresponding to $R = \Lambda/2$ and the dispersion relation computed by Ferrando *et al.* using a very accurate, full vectorial numerical method—the plane-wave expansion method [8]. Further details on the comparison between this method and ours will be presented in the section after the next one. On the contrary, we note large discrepancies between the vectorial results on one side (ours and those from [8]) and, on the other side, those obtained using either a semianalytic scalar theory taken from [4], or a scalar finite-difference scheme [5]. Also note that, if we choose for the boundary a larger radius (in particular, the dashed curve refers to the circle passing through the hexagon vertices), then the results given by our technique depart from those given by [8], which, in our opinion, are the most accurate published so far.

We know from the literature [6] that the difference between vector and scalar approaches becomes much less pronounced, if what one aims at is the dispersion curve of a mode guided by a lattice defect. The different behavior of scalar approaches, when applied to these two problems, may be explained, at least in part, as follows. Compared to a vector approach, a scalar theory underestimates the influence of sharp index discontinuities on the EM-field. A mode guided by a defect in the lattice is mainly confined within a region where the index is constant, and senses index discontinuities only through its small evanescent tails. The cladding mode that we are investigating, on the contrary, spreads out throughout the whole lattice, hence it is influenced by sharp index changes located where most of its energy is located. This may also explain why discrepancies between scalar and vector approaches is wavelength sensitive, and also why the results of

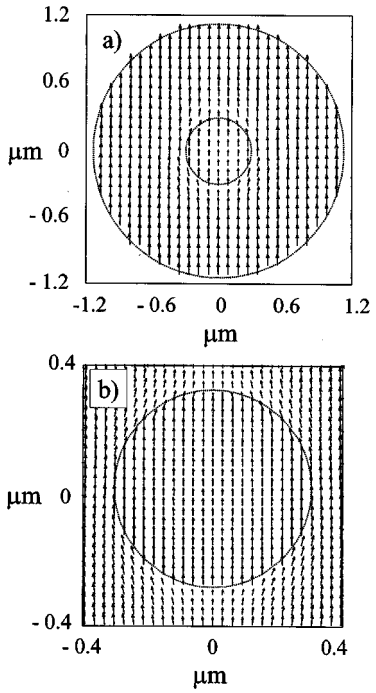

Fig. 5. Transverse electric field vectors for the fundamental mode at the wavelength $\lambda = 1.5$ μm. Panel (b) is an expanded view of panel (a).

our method becomes closer to the scalar ones if we choose a radius R which yields a higher filling factor, i.e., reduces the effect of air holes.

A. Field Profile of the Space Filling Mode

Once the characteristic equation has been solved, we can go back to (3) and (4), and find the transverse field of the space filling mode. Fig.5 shows the flow lines of the transverse electric field vector, for the $EH_{11}^{(T)}$ mode, at $\lambda = 1.5$ μm. We see that it is essentially a linearly polarized field. Part b) is a blow-up of the central region of part a); its purpose is to stress the minute deviations from linear polarization along the y axis that are experienced near the air-silica interface.

Fig.6 shows amplitude contour plots of the x (part a) and y (part b) components of the electric field of the fundamental mode. Note the four-lobe pattern of the small component, strongly reminiscent of the HE_{11} mode of a step-index fiber (the lobes change sign across the verical and horizontal planes of symmetry). This property is preserved, as expected, when the hole at the center of the lattice is filled up with silica, then low butt-coupling loss can be predicted between a holey fiber, and a standard single-mode fiber.

Finally, Fig. 7 shows the linear polarization ratio (LPR) of the fundamental mode. It reconfirms that it is essentially a y polarized mode, with an LPR which decreases at large wavelengths.

These figures, in particular Fig. 5, easily explain why the fundamental mode is two-fold degenerate, as we pointed out in the previous section. In fact, given the symmetry of the boundary conditions on the circle C, our y polarized field must have an x polarized twin. Still, the hexagonal cell we started from does not exhibit a quadrant symmetry. Hence, one might wonder whether the two-fold mode degeneracy is an

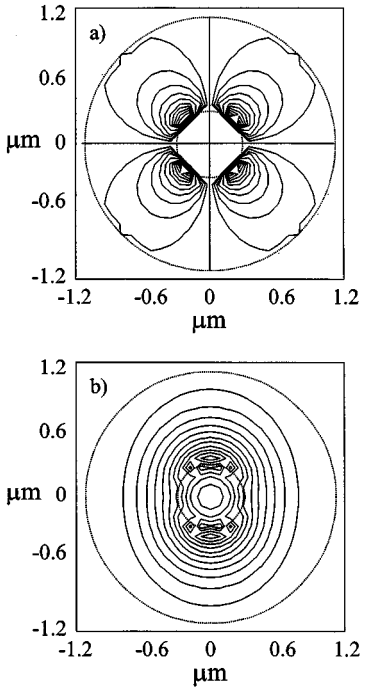

Fig. 6. Contour plots of transverse electric field of the fundamental mode. The mode is y polarized, as in Fig. 5.(a) E_x field. (b) E_y field.

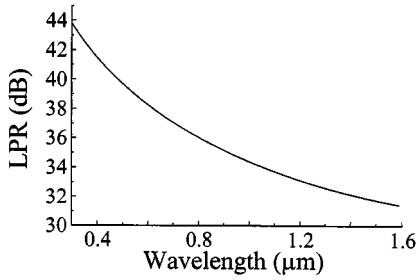

Fig. 7. Linear polarization ratio (LPR) vs. wavelength for the fundamental mode.

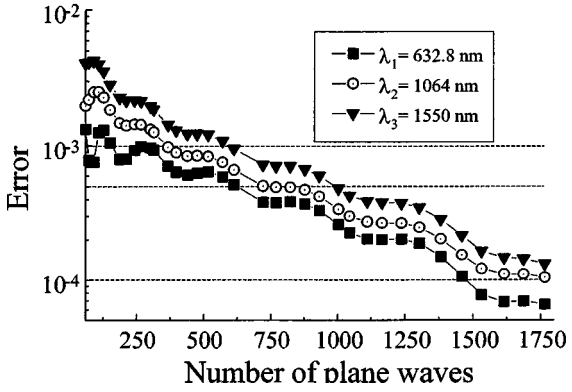

Fig. 8. Absolute error of the space filling mode effective index computed by a fully vectorial plane wave expansion method versus the number of plane waves used in the field expansion.

artefact, introduced by our boundary conditions. Actually, the degeneracy is real: the hexagonal structure cannot distinguish between right-handed and left-handed circular polarizations. Or in other words, as pointed out by one referee, rotation of a mode pattern by $\pi/3$ radians around the z-axis generates another mode, degenerate with the previous one. The two modes are not orthogonal, but are linearly independent and therefore they can be orthogonalized.

B. Comparison with the Plane Wave Expansion Method

One useful consequence of the availability of rigorous analytical expressions for the computation of the SFM effective index in the hexagonal lattice is the possibility of estimating the accuracy of numerical models that are customarily used for wave propagation in photonic crystal fibers. In particular, the method whose accuracy we are going to check here is the so-called "plane wave expansion method": the field is represented as a sum of plane waves whose wave vectors belong to the set of centers of the reciprocal lattice, and Maxwell's equations are replaced by a homogeneous system of linear equations where the unknown coefficients are the amplitude of the plane waves used for the field expansion, and the corresponding propagation vector. As discussed in [10], the computation of the effective index with this method requires the diagonalization of a matrix twice as large as the number of plane waves used in the expansion of each field component.

To get insight on the accuracy of this method, we implemented it and computed the effective index of the space filling mode for a lattice with the same parameters as at $\lambda_1 = 632.8$ nm, $\lambda_2 = 1064$ nm and $\lambda_3 = 1550$ nm. The number of plane waves ranged from $n_{\rm plw} = 61$ to $n_{\rm plw} = 1765$. Fig. 8 shows the results of our comparison between the plane wave numerical method and our analytical method, in terms of the error we found for the various cases. We see that the accuracy of the numerical method depends strongly on the wavelength, and decreases for increasing wavelengths. For instance, for an accuracy of 5×10^{-4} in the evaluation of the cladding index, an expansion over $n_{\rm plw} \simeq 600$ is required at $\lambda = 632.8$ nm; the number grows to $n_{\rm plw} \simeq 720$ for $\lambda = 1064$ nm, and to $n_{\rm plw} \simeq 980$ for $\lambda = 1550$ nm.

V. Conclusion

We investigated the guiding properties of an infinitely self similar dielectric structure, where low-index holes are embedded in a high-index substrate to form a hexagonal lattice. By resorting to simple symmetry considerations, we solved analytically, for the first time, Maxwell's equations in the lattice, in a closed form. This allowed us to provide analytical formulas to derive the dispersion relations of all the modes that may be guided by the structure and, in particular, that of the fundamental mode, often referred to as the "space filling mode".

The expressions we found were also used to analyze the electromagnetic nature of the SFM, and to give a quantitative extimate of the accuracy of the *plane wave expansion* technique, a numerical model which is widely used to study holey fibers. Our results indicate that, in a silica air-lattice having a pitch-to-wavelength ratio of about 1.5, field expansion over roughly 1000 plane waves is required to get a 5×10^{-4} accuracy in the extimation of the mode effective index. Increasing the ratio to values around 2 or around 4, the same set of plane waves provides an

extimated effective index with an error equal to 3.8×10^{-4} and 2.7×10^{-4}, respectively.

ACKNOWLEDGMENT

The authors would like to thank A. Ferrando for providing the data corresponding to the numerically evaluated cladding index curve in Fig. 1, [8], and A. Galtarossa for fruitful discussions and comments. They also thank the referees for their comments, which entailed significant improvements in the presentation.

REFERENCES

[1] S. E. Barkou, J. Broeng, and A. Bjarklev, "Silica-air photonic crystal fiber design that permits waveguiding by a true photonic bandgap effect," *Opt. Lett.*, vol. 24, pp. 46–48, Jan. 1999.

[2] J. Broeng, D. Mogilevstev, S. E. Barkou, and A. Bjarklev, "Photonic crystal fibers: A new class of optical waveguides," *Opt. Fiber Technol.*, vol. 5, pp. 305–330, July 1999.

[3] J. Broeng, T. Sondergaard, S. E. Barkou, P. M. Barbeito, and A. Bjarklev, "Waveguidance by the photonic bandgap effect in optical fibers," *J. Opt. A—Pure Appl. Opt.*, vol. 1, pp. 477–482, July 1999.

[4] T. A. Birks, J. C. Knight, and P. S. J. Russel, "Endlessy single-mode photonic crystal fiber," *Opt. Lett.*, vol. 22, pp. 961–963, July 1997.

[5] M. P. Singh, M. Midrio, A. D. Capobianco, and C. G. Someda, Study of photonic crystal fibers using the scalar finite difference method, in Opt. Lett.. Submitted for publication in.

[6] T. Monro, D. J. Richardson, N. G. B. Broderick, and P. J. Bennett, "Holey optical fibers: An efficient modal model," *J. Lightwave Technol.*, vol. 17, pp. 1093–1102, June 1999.

[7] E. Silvestre, M. V. Andrés, and P. Andrés, "Biorthonormal-basis method for the vector description of optical fiber modes," *J. Lightwave Technol.*, vol. 16, pp. 923–928, May 1998.

[8] A. Ferrando, E. Silvestre, J. J. Miret, P. Andrés, and M. V. Andrés, "Full-vector analysis of a realistic photonic crystal fiber," *Opt. Lett.*, vol. 24, pp. 276–278, Mar. 1999.

[9] C. G. Someda, *Electromagnetic Waves*. London, U.K.: Chapman and Hall, 1998, ch. 10.

[10] A. A. Maradudin and A. R. McGurn, "Out of plane propagation of electromagnetic waves in two-dimensional periodic dielectric medium," *J. Mod. Opt.*, vol. 41, pp. 275–284, 1994.

Michele Midrio, photograph and biography not available at the time of publication.

Mukesh P. Singh, photograph and biography not available at the time of publication.

Carlo G. Someda, photograph and biography not available at the time of publication.